

Article

MXene Boosted CoNi-ZIF-67 as Highly Efficient Electrocatalysts for Oxygen Evolution

Yangyang Wen ^{*}, Zhiting Wei, Chang Ma, Xiaofei Xing , Zhenxing Li ^{*} and Dan Luo ^{*}

State Key Laboratory of Heavy Oil Processing, College of New Energy and Material, Beijing Key Laboratory of Biogas Upgrading Utilization, China University of Petroleum (Beijing), Beijing 102249, China; WZT1215385749@126.com (Z.W.); machang_cup@126.com (C.M.); xingxiaofei_cup@126.com (X.X.)

^{*} Correspondence: wenyangyang@cup.edu.cn (Y.W.); lizx@cup.edu.cn (Z.L.); luodan@iccas.ac.cn (D.L.)

Received: 19 April 2019; Accepted: 15 May 2019; Published: 20 May 2019



Abstract: Oxygen evolution reaction (OER) is a pivotal step for many sustainable energy technologies, and exploring inexpensive and highly efficient electrocatalysts is one of the most crucial but challenging issues to overcome the sluggish kinetics and high overpotentials during OER. Among the numerous electrocatalysts, metal-organic frameworks (MOFs) have emerged as promising due to their high specific surface area, tunable porosity, and diversity of metal centers and functional groups. It is believed that combining MOFs with conductive nanostructures could significantly improve their catalytic activities. In this study, an MXene supported CoNi-ZIF-67 hybrid (CoNi-ZIF-67@Ti₃C₂T_x) was synthesized through the in-situ growth of bimetallic CoNi-ZIF-67 rhombic dodecahedrons on the Ti₃C₂T_x matrix via a coprecipitation reaction. It is revealed that the inclusion of the MXene matrix not only produces smaller CoNi-ZIF-67 particles, but also increases the average oxidation of Co/Ni elements, endowing the CoNi-ZIF-67@Ti₃C₂T_x as an excellent OER electrocatalyst. The effective synergy of the electrochemically active CoNi-ZIF-67 phase and highly conductive MXene support prompts the hybrid to process a superior OER catalytic activity with a low onset potential (275 mV vs. a reversible hydrogen electrode, RHE) and Tafel slope (65.1 mV·dec⁻¹), much better than the IrO₂ catalysts and the pure CoNi-ZIF-67. This work may pave a new way for developing efficient non-precious metal catalyst materials.

Keywords: oxygen evolution reaction; metal-organic frameworks; MXene; Ti₃C₂T_x; hybrid

1. Introduction

With the rapid combustion of fossil fuels and the ever-growing concerns relating to the environmental crisis, developing sustainable energy technologies (such as metal-air batteries and water splitting) has triggered extensive attention [1]. Oxygen evolution reaction (OER) is the key process for these electricity-driven devices, but it has been significantly hindered by its sluggish kinetics and substantial overpotential [2]. Therefore, highly active electrocatalysts are required to increase the reaction rate and to lower the overpotentials in the OER process. To date, the precious metal oxides (e.g., RuO₂ and IrO₂) are the best electrocatalysts with a promoted proton-coupled charge transfer process, but their scale-up implementation has been greatly hampered by their high price, scarcity and poor durability [3,4]. Within this context, increasing efforts have been devoted to the exploration of inexpensive, earth-abundant and highly efficient electrocatalysts for OER [5]. Among them, the earth-based transition metal-rich compounds, including transition metal oxides [3], sulfides [6] and phosphides [7], have exhibited great promise as OER electrocatalysts.

Recently, metal organic frameworks (MOFs) consisting of the coordination of organic ligands and metal ions or clusters have received increasing attention for catalysis-related applications [4,8]. MOFs are an important class of porous solids in electrocatalysis in view of their high specific surface

area, tunable porosity, and diversity of metal centers and functional groups [9]. However, it is still a challenge to directly utilize MOFs as efficient OER electrocatalysts because of their poor conductivity. One commonly-used strategy is adopting MOFs as precursors to prepare metal-based compounds/porous carbon composites via a high-temperature pyrolysis. However, the active sites and intrinsic structure of MOFs are inevitably sacrificed with the loss of organic ligands during the pyrolysis [10]. Another possible strategy is to combine MOFs with conductive nanostructures, which has demonstrated a significant enhancement in the electrocatalytic properties [11,12].

MXene is a new class of two-dimensional materials, synthesized by selectively etching A layers from its MAX phase [13]. It can be represented using a formula of $M_{n+1}X_nT_x$, where M is the early transition metal, X stands for C and/or N elements, and T for the surface terminations (–O, –F or –OH) [14]. MXene has emerged as a promising nanomaterial in various fields, including energy storage [15,16], energy conversion [11,17], water purification [18], electromagnetic interference [19], and so on, owing to its excellent electrical conductivity and surface hydrophilicity. Besides, MXene also demonstrated the possibility of being an excellent support by altering the electrophilicity of active centers in the supported catalysts and thus modifying the catalytic activity of the composites [20].

In this work, a MXene supported CoNi-ZIF-67 hybrid (CoNi-ZIF-67@Ti₃C₂T_x) was synthesized by the in-situ growth of bimetallic CoNi-ZIF-67 rhombic dodecahedrons on the Ti₃C₂T_x matrix via a coprecipitation reaction. The effective synergy of the CoNi-ZIF-67 and MXene phases endows the hybrid with a remarkable electrocatalytic activity for OER, with a low onset potential (275 mV vs. a reversible hydrogen electrode, RHE) and Tafel slope (65.1 mV·dec^{−1}).

2. Materials and Methods

2.1. Preparation of Ti₃C₂T_x MXene

Ti₃AlC₂ powder was first prepared via the HF-etching method [21]. Briefly, 1 g of Ti₃AlC₂ powder was blended with 40 mL of 40 wt.% HF solution under continuous stirring at 45 °C for 24 h. The resulting suspension was separated by centrifugation, washed several times with distilled water, and freeze-dried, obtaining the accordion-like Ti₃C₂T_x MXene.

2.2. Preparation of CoNi-ZIF-67@Ti₃C₂T_x and Pure CoNi-ZIF-67

Typically, 300 mg Ti₃C₂T_x, 0.9 mmol Co(NO₃)₂·6H₂O and 0.1 mmol Ni(NO₃)₂·6H₂O were dispersed in 8 mL methanol under sonication for 1 h. Then, 8 mmol of 2-methylimidazole was dissolved in another 8 mL methanol under stirring for 30 min. The two above solutions were mixed together, followed by adding 2 mg of hexadecyl trimethyl ammonium bromide (CTAB) and continuously stirring for 8 h at room temperature. The final precipitates were collected by centrifugation, washed with methanol and water several times, and dried at 60 °C under vacuum for 12 h. As a control, pure CoNi-ZIF-67 was prepared via the same procedure but without adding the Ti₃C₂T_x.

2.3. Materials Characterizations

The morphology and structure of the as-prepared catalysts were characterized by scanning electron microscopy (SEM, Hitachi SU8010, Tokyo, Japan), transmission electron microscopy (TEM, JEM 2100 LaB6, Tokyo, Japan), powder X-ray diffractometer analysis (XRD, Bruker D8 Advance instrument, Karlsruhe, Germany) with a Cu K α irradiation source at a scanning rate of 1° per min, and X-ray photoelectron spectroscopy (XPS, PHI5000 Versaprobe, Kanagawa, Japan) with an Al K α X-ray source. The binding energies of the XPS measurements were calibrated to the C 1s peak at 285.0 eV. The specific surface areas and pore size distribution of the catalysts were conducted on the ASAP2460 Surface Area and Porosity Analyzer (Micromeritics, Atlanta, GA, USA). The surface areas (S_{BET}) were calculated from the N₂ sorption isotherms via the Brunauer-Emmett-Teller method, and the pore size distributions were calculated from the N₂ isotherms using the non-local density functional theory (NLDFT) method.

2.4. Electrode Preparation and Electrochemical Measurements

All electrocatalytic performances were evaluated on a CHI 760E electrochemical workstation (Chenhua Instrument, Shanghai, China) with a standard three-electrode system in 0.1 M KOH aqueous solution at room temperature. A glassy carbon electrode (GCE, 5 mm in diameter) coated with the as-prepared catalysts was employed as the working electrode, a Hg/HgO electrode as the reference electrode and a graphite rod as the counter electrode. Before the test, the catalyst ink was prepared by dispersing 10 mg of catalyst powder in a mixture of 40 μL 5 wt.% Nafion solution (Sigma-Aldrich, Shanghai, China), 750 μL water and 250 μL ethanol. After ultrasonication for 30 min, 10 μL of the catalyst ink was pipetted onto the freshly-polished GCE with a catalyst mass loading of $\sim 0.5 \text{ mg}_{\text{cat}} \cdot \text{cm}^{-2}$. All the potentials were calibrated to a reversible hydrogen electrode (RHE) according to the equation, $E(\text{RHE}) = E(\text{Hg}/\text{HgO}) + 0.059\text{pH} + 0.098$. Before the electrochemical measurement, the electrolyte was bubbled with an O_2 flow for 30 min, and a gas flow was maintained over the electrolyte during the measurement to ensure the O_2 saturation. The polarization curves were tested using the linear sweep voltammetry (LSV) at a scan rate of $50 \text{ mV} \cdot \text{s}^{-1}$. The double-layer capacitance (C_{dl}) was calculated from the cyclic voltammetry (CV) curves in a small potential range of 1.023–1.073 V vs. RHE without the occurrence of an apparent faradic process. The plots of the current density difference [$\Delta j = (j_{\text{a}} - j_{\text{c}})$], at 1.048 V vs. RHE against the scan rates of 10–60 $\text{mV} \cdot \text{s}^{-1}$, were linearly fitted, and the slope is the C_{dl} of the catalysts. Electrochemical impedance spectroscopy (EIS) was carried out at 1.46 V vs. RHE in a frequency range of 0.1– 10^5 Hz. For the stability test, the catalysts were performed at 1.46 V vs. RHE over a 20,000 s continuous time. In comparison, the commercial IrO_2 catalyst purchased from Sigma-Aldrich with the same catalyst mass loading was tested under the same conditions.

3. Results

The preparation procedure of $\text{CoNi-ZIF-67@Ti}_3\text{C}_2\text{T}_x$ is illustrated in Figure 1. In brief, the accordion-like $\text{Ti}_3\text{C}_2\text{T}_x$ was first prepared by the selective etching of Al layers from the Ti_3AlC_2 MAX phase using HF. Then, Co^{2+} and Ni^{2+} ions with 2-methylimidazole in methanol were added. The bimetallic CoNi-ZIF-67 could grow in-situ on the $\text{Ti}_3\text{C}_2\text{T}_x$ via a coprecipitation reaction. Considering the negatively charged $\text{Ti}_3\text{C}_2\text{T}_x$ surface due to the presence of numerous surface termination groups (e.g., $-\text{O}$, $-\text{OH}$, and $-\text{F}$) introduced during the etching process, Co^{2+} and Ni^{2+} ions could be easily adsorbed on these termination group sites by electrostatic interaction, and could in-situ synthesize CoNi-ZIF-67 rhombic dodecahedrons on the surface and between the interlayers of $\text{Ti}_3\text{C}_2\text{T}_x$.

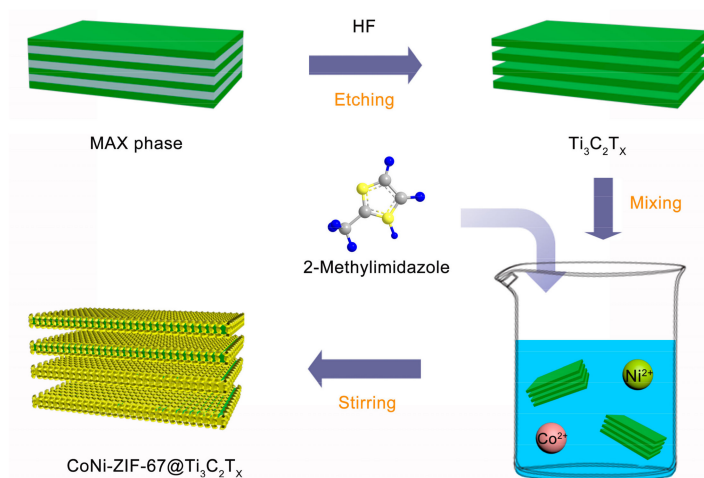


Figure 1. Schematic illustration of the preparation of $\text{CoNi-ZIF-67@Ti}_3\text{C}_2\text{T}_x$.

The XRD analysis was investigated for the structural characterization of the pristine $\text{Ti}_3\text{C}_2\text{T}_x$, $\text{CoNi-ZIF-67@Ti}_3\text{C}_2\text{T}_x$, and pure CoNi-ZIF-67. As shown in Figure 2a (enlarged image in Figure S1),

the XRD pattern of the pristine $\text{Ti}_3\text{C}_2\text{T}_x$ represents the characteristic strong peak of the (002) plane at 8.2° , and the weak peaks of the (004), (101) and (110) planes according to the JCPDS card no. 52-0875, confirming the successful preparation of the $\text{Ti}_3\text{C}_2\text{T}_x$ phases. The pure CoNi-ZIF-67 shows the typical sharp peaks, consistent with the reported literatures [22]. The XRD pattern of the CoNi-ZIF-67@ $\text{Ti}_3\text{C}_2\text{T}_x$ hybrid displays a superimposition of the two phases, featured with four obvious peaks at 6.6° of the (002) plane and 61.2° of the (110) plane for $\text{Ti}_3\text{C}_2\text{T}_x$, and 7.4° of the (011) plane and 12.8° of the (112) plane for CoNi-ZIF-67, revealing the effective combination of the CoNi-ZIF-67 and $\text{Ti}_3\text{C}_2\text{T}_x$ phases. It notes that an apparent shift of the (002) plane to a lower angle was detected in the CoNi-ZIF-67@ $\text{Ti}_3\text{C}_2\text{T}_x$, compared with the pristine $\text{Ti}_3\text{C}_2\text{T}_x$ phase. This left-shift suggests a c-lattice parameter change from 2.16 nm in $\text{Ti}_3\text{C}_2\text{T}_x$ to 2.68 nm in the hybrid, disclosing the intercalation of the $\text{Ti}_3\text{C}_2\text{T}_x$ layers due to the inclusion of the CoNi-ZIF-67 particles.

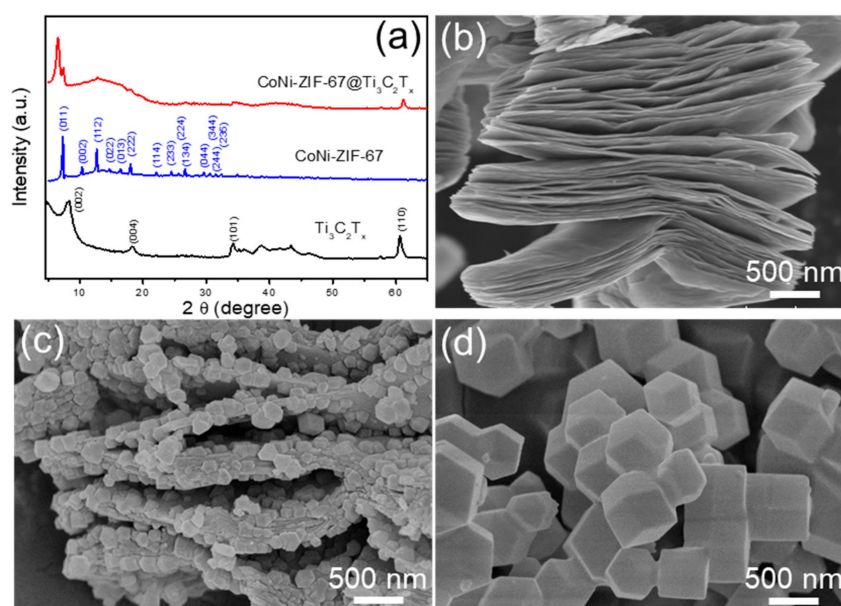


Figure 2. (a) X-ray diffraction (XRD) patterns of $\text{Ti}_3\text{C}_2\text{T}_x$, CoNi-ZIF-67@ $\text{Ti}_3\text{C}_2\text{T}_x$, and pure CoNi-ZIF-67. Scanning electron microscopy (SEM) images of (b) $\text{Ti}_3\text{C}_2\text{T}_x$; (c) CoNi-ZIF-67@ $\text{Ti}_3\text{C}_2\text{T}_x$, and (d) pure CoNi-ZIF-67.

The morphology of the as-prepared catalysts was characterized by SEM and TEM, revealing the hybrid structure of CoNi-ZIF-67@ $\text{Ti}_3\text{C}_2\text{T}_x$. Figure 2b shows the SEM image of the pristine $\text{Ti}_3\text{C}_2\text{T}_x$, showing the typical accordion-like structure. The CoNi-ZIF-67@ $\text{Ti}_3\text{C}_2\text{T}_x$ hybrid remains a multilayered structure as the pristine $\text{Ti}_3\text{C}_2\text{T}_x$ but attached with numerous small particles with a size of 100–200 nm between the interlayers of $\text{Ti}_3\text{C}_2\text{T}_x$ (Figure 2c). During the HF etching process, Al layers were removed from the MAX phase, and Ti atoms were bonded with the surface functional groups (–O, –OH, or –F), conferring the $\text{Ti}_3\text{C}_2\text{T}_x$ with negatively charged surfaces [23], which would facilitate the absorption of positively charged Co^{2+} and/or Ni^{2+} ions and subsequently coordinate with 2-methylimidazole molecules for an in-situ synthesis of the CoNi-ZIF-67 particles [11]. As a result, a significant intercalation of the $\text{Ti}_3\text{C}_2\text{T}_x$ layers is observed in Figure 2c due to the inclusion of the CoNi-ZIF-67 particles. Figure 2d presents the SEM image of the pure CoNi-ZIF-67, showing the typical rhombic dodecahedral structure of CoNi-ZIF-67 and a uniform particle size of 400–600 nm. Particularly, the CoNi-ZIF-67 particles grown on the $\text{Ti}_3\text{C}_2\text{T}_x$ surface are much smaller than the pure CoNi-ZIF-67 particles (Figure 2c,d). It is speculated that the $\text{Ti}_3\text{C}_2\text{T}_x$ matrix reduced the aggregation of CoNi-ZIF-67 and deterred the particle growth of CoNi-ZIF-67. In the preparation process, CTAB was added as a sealing agent to aid the formation of smaller and uniform CoNi-ZIF-67 particles. Figure S2 shows the SEM images of two CoNi-ZIF-67 catalysts with CTAB and without CTAB. It can be seen that the CoNi-ZIF-67 particles

using CTAB are in the range of 400–600 nm (Figure S2a,b), while the CoNi-ZIF-67 without CTAB exhibits a relatively wider particle size range, from 300 nm to 1 μm (Figure S2c,d). Besides, it is revealed that the CTAB could also facilitate the intercalation of the CoNi-ZIF-67 particles into the interlayers of $\text{Ti}_3\text{C}_2\text{T}_x$ (Figure S3).

The TEM images in Figure 3 confirm the hybrid structure of $\text{CoNi-ZIF-67@Ti}_3\text{C}_2\text{T}_x$ and the rhombic dodecahedral structure of pure CoNi-ZIF-67. Compared with the accordion-like structure of $\text{Ti}_3\text{C}_2\text{T}_x$, the composite maintained the multilayered structure but was firmly attached with numerous particles on the surface and between the interlayers of $\text{Ti}_3\text{C}_2\text{T}_x$. It should be noted that the pristine MXene shows obvious lattice fringes for the layers (Figure 3b), while the lattice fringes were not observed in the $\text{CoNi-ZIF-67@Ti}_3\text{C}_2\text{T}_x$ (Figure 3d). We speculate that the MXene is coated with a thick layer of CoNi-ZIF-67 in the hybrid, and that it is therefore not as easy to observe the lattice fringes in the hybrid as in the pristine MXene. In addition, the high-angle annular dark-field scanning transmission electron microscopy (HAADF-STEM) and EDX elemental mapping images of the $\text{CoNi-ZIF-67@Ti}_3\text{C}_2\text{T}_x$ hybrid demonstrate the distribution of C, Co and Ni elements on the surface of MXene (Figure S4).

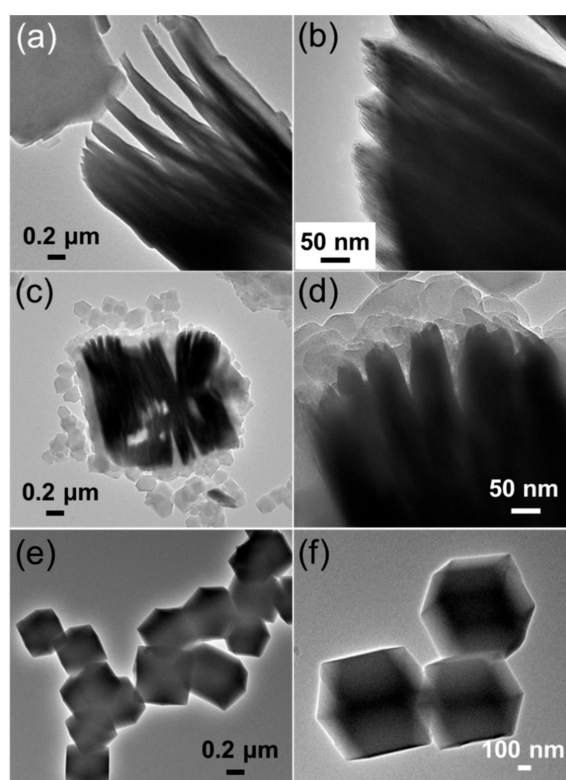


Figure 3. Transmission electron microscopy (TEM) images of (a,b) $\text{Ti}_3\text{C}_2\text{T}_x$, (c,d) $\text{CoNi-ZIF-67@Ti}_3\text{C}_2\text{T}_x$, and (e,f) pure CoNi-ZIF-67 at different magnifications.

The porosity of the as-prepared catalysts was measured by nitrogen adsorption isotherms, as shown in Figure S5a. The specific surface areas (S_{BET}) for $\text{Ti}_3\text{C}_2\text{T}_x$, $\text{CoNi-ZIF-67@Ti}_3\text{C}_2\text{T}_x$, and pure CoNi-ZIF-67 were 14.1, 202.9, and 1135.8 $\text{m}^2\cdot\text{g}^{-1}$, respectively. The pure CoNi-ZIF-67 exhibits a dominant pore size of 1.08 and 1.3 nm, while the $\text{CoNi-ZIF-67@Ti}_3\text{C}_2\text{T}_x$ provides a larger dominant pore size of 1.74 nm (Figure S5b–d).

The XPS analysis further confirms the co-existence of C, Ti, Co and Ni elements in the $\text{CoNi-ZIF-67@Ti}_3\text{C}_2\text{T}_x$, with the elemental contents of 50.4, 11.2, 2.9 and 0.3 at.%, respectively (Table S1). The high resolution C 1s spectrum in Figure 4a can be deconvoluted into four peaks at 282.0, 285.0, 285.5 and 286.5 eV, which are attributed to the C–Ti, C=C, C–C and C–O species [11], respectively. The Ti region shows two pairs of $2p_{3/2}/2p_{1/2}$ doublets for the Ti–C (455.6 eV) and Ti–O (457.3 eV) species [21]. The Co 2p spectrum features three prominent species: Co^{2+} (782.6 eV for $2p_{3/2}$), Co^{3+}

(781.5 eV for $2p_{3/2}$) and satellite (787.2 eV) [24]. The MXene has an abundant number of surface termination groups (e.g., $-O$, $-OH$, and $-F$), which could adsorb the Co^{2+}/Ni^{2+} ions on the MXene surface and may change the Co/Ni oxidation during the pyrolysis process in the inert atmosphere. Consequently, the high-resolution Co/Ni XPS fitting may be helpful for explaining this part. The noise of the Co/Ni region is relatively high due to their low concentrations (Figure 4c,d). Consequently, we fitted the XPS data within the fitting error ($\sum \chi^2$) below 2. The Ni 2p region was analyzed into Ni^{2+} (855.0 eV for $2p_{3/2}$), Ni^{3+} (856.7 eV for $2p_{3/2}$) and satellite (861.1 eV) [25]. The core level peak analyses for the Co and Ni elements were listed in Tables S2 and S3. Interestingly, the $CoNi-ZIF-67@Ti_3C_2T_x$ exhibits a relatively higher ratio for the Co^{3+}/Co^{2+} species than the pure CoNi-ZIF-67 does, and the same trend can be observed in the Ni elements (Figure S6). We speculate that the introduction of MXene leads to the oxidation of the Co and Ni species in the CoNi-ZIF-67 phases, which may result from the numerous surface terminations on the MXene ($-O$ or $-OH$), and which thus indicates the interaction between the MXene substrate and the in-situ grown CoNi-ZIF-67 phases.

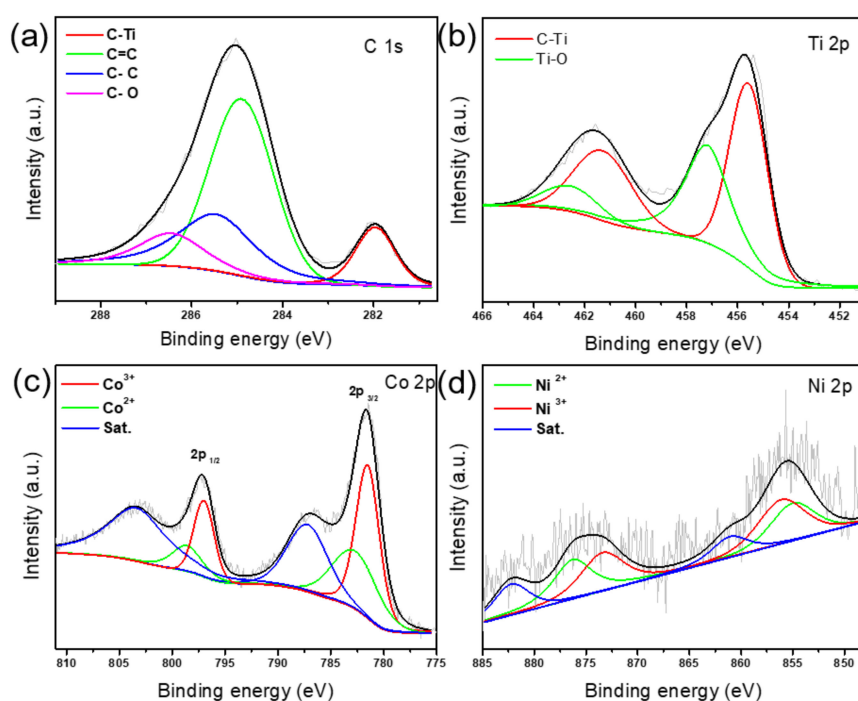


Figure 4. High resolution X-ray photoelectron spectroscopy (XPS) spectrum of (a) C 1s; (b) Ti 2p; (c) Co 2p and (d) Ni 2p for $CoNi-ZIF-67@Ti_3C_2T_x$.

The electrocatalytic activity of the as-prepared catalysts was first evaluated in a 0.1 M KOH solution in a standard three-electrode cell. Figure 5a presents the iR -corrected linear sweep voltammetry (LSV) curves at a scan rate of $50 \text{ mV}\cdot\text{s}^{-1}$. It is apparent that the $Ti_3C_2T_x$ has no OER activity. Meanwhile, the $CoNi-ZIF-67@Ti_3C_2T_x$ hybrid shows an enhanced electrocatalytic activity with a much larger current density than the pure CoNi-ZIF-67, which confirms the positive effect of the $Ti_3C_2T_x$ matrix on enhancing the OER activity. Accordingly, the $CoNi-ZIF-67@Ti_3C_2T_x$ displays a lower onset overpotential of 275 mV than the pure CoNi-ZIF-67 does (341 mV). The OER activity is also better than that of the as-purchased IrO_2 catalyst, with an onset potential of 281 mV, which indicates the good electrocatalytic performance of the $CoNi-ZIF-67@Ti_3C_2T_x$ hybrid. Another critical indicator of the OER activity is the overpotential at a current density of $10 \text{ mA}\cdot\text{cm}^{-2}$ ($\eta_j = 10$), which is generally attributed to an approximately 10% efficient solar-to-fuel conversion device [23]. As listed in Figure 5b, the $CoNi-ZIF-67@Ti_3C_2T_x$ shows the lowest $\eta_j = 10$ value (323 mV), when compared to the CoNi-ZIF-67 (389 mV) and IrO_2 catalysts (345 mV). It can be seen that the pure CoNi-ZIF-67 exhibited a poor catalytic performance, when compared to the as-purchased IrO_2 catalyst, which is mainly related to the instinct

poor conductivity of the CoNi-ZIF-67, and which thus demonstrates the contribution of the MXene matrix to the good OER activity in the composite. Besides, in view of the XPS analysis (Tables S1–S3), no obvious changes in the Co/Ni atomic ratio, other than an apparent increase in the average oxidation state of both the Co and Ni elements, were detected after introducing the MXene matrix in the CoNi-ZIF-67 phase. We speculated that the enhanced OER activity of CoNi-ZIF-67@Ti₃C₂T_x may also be related to the altering of the oxidation state of the transmission metal (Co and Ni) active sites [23].

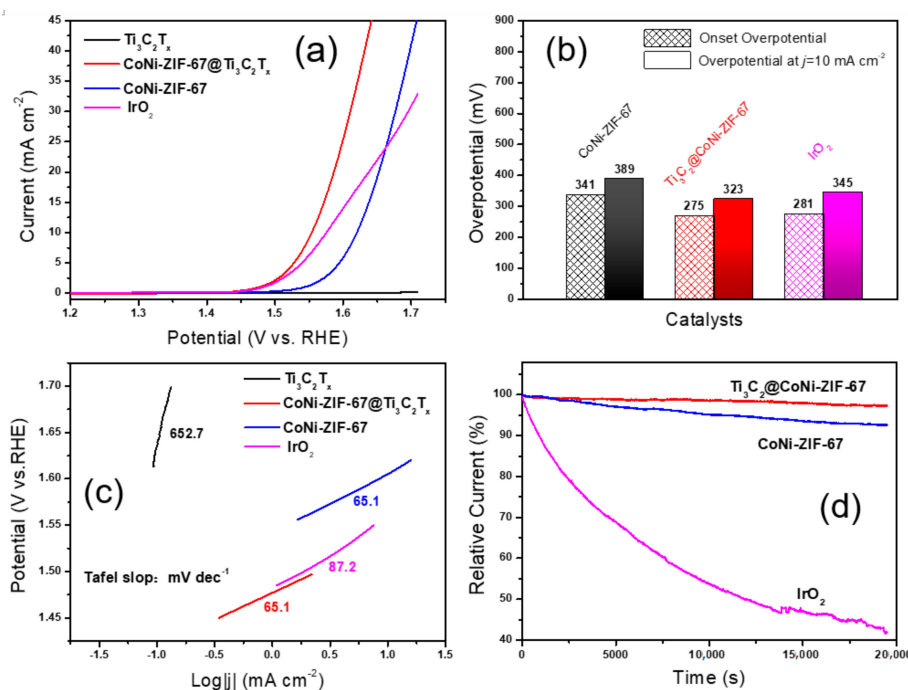


Figure 5. (a) Linear sweep voltammetry (LSV) curves of the catalyst Ti₃C₂T_x, CoNi-ZIF-67@Ti₃C₂T_x, pure CoNi-ZIF-67 and IrO₂ at 50 mV·s⁻¹; (b) A comparison of the catalysts in the onset potential and overpotential at a current density of 10 mA·cm⁻²; (c) Tafel plots of the different catalysts; and (d) Chronoamperometry curves at 1.46 V vs. RHE over a 20,000 s continuous time.

The Tafel slope is a pivotal parameter for providing insightful information on the OER mechanism, particularly for the elucidation of OER kinetics and the rate-determining step [1]. In this regard, the Tafel slopes of the catalysts were plotted in Figure 5c. The value for CoNi-ZIF-67@Ti₃C₂T_x is 65.1 mV·dec⁻¹, much smaller than that of the as-purchased IrO₂ catalyst (87.2 mV·dec⁻¹), thus revealing the higher OER rate and favorable kinetics of the CoNi-ZIF-67@Ti₃C₂T_x hybrid. However, it should be noted that, in our work, the Tafel plot of the as-purchased IrO₂ catalyst is higher than that of the reported nano-sized IrO₂ catalyst [26], which may be related to the morphology or size of the as-purchased IrO₂ in the reported works. Additionally, a comparison of the OER performance between the recently reported CoNi-based electrocatalysts with the CoNi-ZIF-67@Ti₃C₂T_x in this work was listed in Table S4, indicating the excellent electrocatalytic properties of the CoNi-ZIF-67@Ti₃C₂T_x.

Furthermore, the durability of the catalysts was also performed at a constant potential of 1.46 V vs. RHE. As shown in the chronoamperometry curves (Figure 5d), the current of the CoNi-ZIF-67@Ti₃C₂T_x hybrid remains nearly constant, with up to a 97.3% retention over a continuous time of 20,000 s, which is much more superior than that of the pure CoNi-ZIF-67 (92.6% retention) and that of the IrO₂ catalyst (only 43.4% remained), demonstrating the excellent stability of the CoNi-ZIF-67@Ti₃C₂T_x.

To better understand the catalytic activity of the CoNi-ZIF-67@Ti₃C₂T_x hybrid, the electrochemically active surface area (ECSA) of the catalysts was investigated. The ECSA is normally positively correlated with the electrochemical double-layer capacitance (C_{dl}) [27]. Therefore, C_{dl} was calculated from the cyclic voltammetry (CV) curves at different scan rates in a narrow potential

range of 1.023–1.073 V vs. RHE (Figure S7). As shown in Figure 6a, CoNi-ZIF-67@Ti₃C₂T_x gives a much higher C_{dI} (5.77 mF·cm⁻²) than the Ti₃C₂T_x (1.18 mF·cm⁻²) and the pure CoNi-ZIF-67 (1.57 mF·cm⁻²) do, indicating a higher ECSA and more active sites in the hybrid. The higher ECSA is consistent with the smaller particle size of CoNi-ZIF-67 in the hybrid, as shown in Figure 2, which would expose more electrochemical active sites with the electrolyte solution. Additionally, the electrochemical impedance spectroscopy measurement was carried out to analyze the interfacial resistance of the electrocatalysts (Figure 6b). The Nyquist plots of the catalysts were fitted by the RC circuit model, as shown in the inset of Figure 6b, including an internal resistance (R1) and a charge transfer resistance (R2) for the electrochemical reaction [28–32]. The simulated R1 and R2 were shown in Table S5, which reveals that CoNi-ZIF-67@Ti₃C₂T_x exhibits a smaller R1 and R2 than the pure CoNi-ZIF-67 and IrO₂, disclosing the optimized charge-transfer capacity of the hybrid during the OER process.

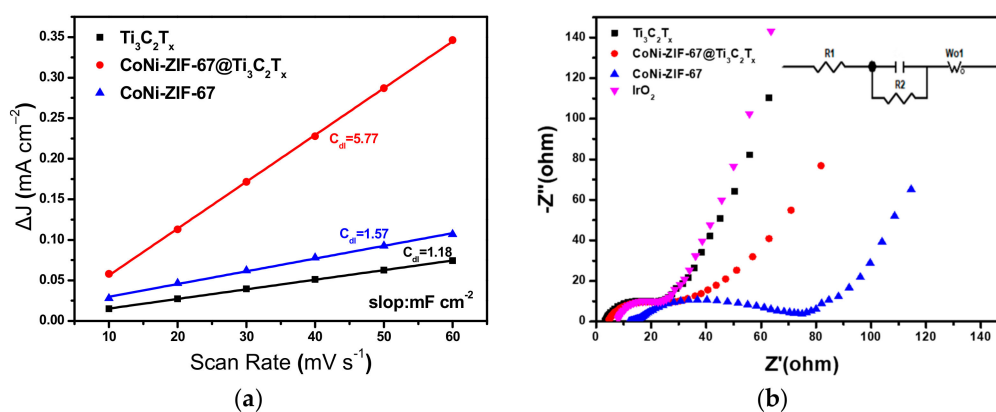


Figure 6. (a) $\Delta J = (J_a - J_c)$ plotted scan rates and (b) Nyquist plots for different catalysts.

4. Conclusions

In summary, a MXene supported CoNi-ZIF-67 hybrid was synthesized via the in-situ growth of CoNi-ZIF-67 rhombic dodecahedrons on the Ti₃C₂T_x matrix via a coprecipitation reaction. It is shown that the addition of CTAB during the preparation process would aid the formation of smaller and uniform CoNi-ZIF-67 particles, while the CTAB could also facilitate the intercalation of CoNi-ZIF-67 particles into the interlayers of Ti₃C₂T_x, forming a hybrid structure composed of two phases. This CoNi-ZIF-67@Ti₃C₂T_x hybrid exhibited a superior OER catalytic activity with a low onset potential (275 mV vs. a reversible hydrogen electrode, RHE) and Tafel slope (65.1 mV·dec⁻¹), much better than that of the IrO₂ catalysts and the pure CoNi-ZIF-67. On the basis of a comprehensive analysis, it is speculated that the good OER activity for the CoNi-ZIF-67@Ti₃C₂T_x hybrid may be attributed to the following factors: (i) an enhanced conductivity of CoNi-ZIF-67 after the inclusion of the MXene matrix, (ii) a hybrid structure with smaller CoNi-ZIF-67 particles, (iii) an increase in the oxidation state of the Co and Ni elements after the introduction of MXene, and (iv) a high electrochemically active surface area for the hybrid. Therefore, the effective synergy shows the hybrid to be an excellent OER electrocatalyst that may pave a new way for the development of efficient non-precious metal electrocatalysts for OER.

Supplementary Materials: The following are available online at <http://www.mdpi.com/2079-4991/9/5/775/s1>, Table S1: Elemental compositions of Catalysts (at.%) determined by XPS, Table S2: Co2p core level peak analyses of catalysts (at.%), Table S3: Ni2p core level peak analyses of catalysts (at.%), Table S4: Comparisons of OER performance between recent reported CoNi-based electrocatalysts with CoNi-ZIF-67@Ti₃C₂T_x, Table S5, The simulated internal resistance (R1) and charge transfer resistance (R2) from the Nyquist plots, Figure S1: Enlarged image of XRD patterns of catalysts, Figure S2: SEM images of pure CoNi-ZIF-67 prepared by the same procedure but with CTAB (a,b) and without CTAB (c,d), Figure S3: SEM image of CoNi-ZIF-67@Ti₃C₂T_x without using CTAB, Figure S4: HAADF-STEM images and the corresponding elemental maps of C, Ti, Co and Ni in the CoNi-ZIF-67@Ti₃C₂T_x, Figure S5: Nitrogen adsorption isotherms and pore size distribution of catalysts, Figure S6:

XPS results of $\text{Ti}_3\text{C}_2\text{T}_x$ and CoNi-ZIF-67, Figure S7: CV curves in a potential range of 1.023–1.073 V vs. RHE of catalysts.

Author Contributions: Y.W. designed the experiments and wrote the paper; Z.L. designed the experiments; Z.W., C.M. and X.X. performed the experiments and analyzed the data, D.L. conducted the work and revised the paper.

Funding: This research was financially supported by Science Foundation of China University of Petroleum, Beijing No. 2462017YJRC013 (Y.W.), No. 2462019BJRC001 (Z.L.), No. 2462018BJB002 (D.L.), Beijing Natural Science Foundation (Grant No. 2182061) (Z.L.) and Beijing Municipal Natural Science Foundation No. 2184119 (D.L.).

Conflicts of Interest: The authors declare no conflict of interest.

References

1. Suen, N.T.; Hung, S.F.; Quan, Q.; Zhang, N.; Xu, Y.J.; Chen, H.M. Electrocatalysis for the oxygen evolution reaction: Recent development and future perspectives. *Chem. Soc. Rev.* **2017**, *46*, 337–365. [[CrossRef](#)] [[PubMed](#)]
2. Osgood, H.; Devaguptapu, S.V.; Xu, H.; Cho, J.; Wu, G. Transition metal (Fe, Co, Ni, and Mn) oxides for oxygen reduction and evolution bifunctional catalysts in alkaline media. *Nano Today* **2016**, *11*, 601–625. [[CrossRef](#)]
3. Ma, T.Y.; Dai, S.; Jaroniec, M.; Qiao, S.Z. Metal-organic framework derived hybrid Co_3O_4 -carbon porous nanowire arrays as reversible oxygen evolution electrodes. *J. Am. Chem. Soc.* **2014**, *136*, 13925–13931. [[CrossRef](#)]
4. Zhao, S.; Wang, Y.; Dong, J.; He, C.T.; Yin, H.; An, P.; Zhao, K.; Zhang, X.; Gao, C.; Zhang, L.; et al. Ultrathin metal-organic framework nanosheets for electrocatalytic oxygen evolution. *Nat. Energy* **2016**, *1*, 16184. [[CrossRef](#)]
5. Zhao, Q.; Yan, Z.; Chen, C.; Chen, J. Spinels: Controlled preparation, oxygen reduction/evolution reaction application, and beyond. *Chem. Rev.* **2017**, *117*, 10121–10211. [[CrossRef](#)] [[PubMed](#)]
6. Qian, H.; Tang, J.; Wang, Z.; Kim, J.; Kim, J.H.; Alshehri, S.M.; Yanmaz, E.; Wang, X.; Yamauchi, Y. Synthesis of cobalt sulfide/sulfur doped carbon nanocomposites with efficient catalytic activity in the oxygen evolution reaction. *Chem. Eur. J.* **2016**, *22*, 18259–18264. [[CrossRef](#)] [[PubMed](#)]
7. Yu, X.Y.; Feng, Y.; Guan, B.; Lou, X.W.; Paik, U. Carbon coated porous nickel phosphides nanoplates for highly efficient oxygen evolution reaction. *Energy Environ. Sci.* **2016**, *9*, 1246–1250. [[CrossRef](#)]
8. Morozan, A.; Jaouen, F. Metal organic frameworks for electrochemical applications. *Energy Environ. Sci.* **2012**, *5*, 9269–9290. [[CrossRef](#)]
9. Lee, J.; Farha, O.K.; Roberts, J.; Scheidt, K.A.; Nguyen, S.T.; Hupp, J.T. Metal-organic framework materials as catalysts. *Chem. Soc. Rev.* **2009**, *38*, 1450–1459. [[CrossRef](#)] [[PubMed](#)]
10. Liu, S.; Wang, Z.; Zhou, S.; Yu, F.; Yu, M.; Chiang, C.Y.; Zhou, W.; Zhao, J.; Qiu, J. Metal-organic-framework-derived hybrid carbon nanocages as a bifunctional electrocatalyst for oxygen reduction and evolution. *Adv. Mater.* **2017**, *29*, 1700874. [[CrossRef](#)]
11. Zhao, L.; Dong, B.; Li, S.; Zhou, L.; Lai, L.; Wang, Z.; Zhao, S.; Han, M.; Gao, K.; Lu, M.; et al. Interdiffusion reaction-assisted hybridization of two-dimensional metal-organic frameworks and $\text{Ti}_3\text{C}_2\text{T}_x$ nanosheets for electrocatalytic oxygen evolution. *ACS Nano* **2017**, *11*, 5800–5807. [[CrossRef](#)]
12. Wang, L.; Wu, Y.; Cao, R.; Ren, L.; Chen, M.; Feng, X.; Zhou, J.; Wang, B. Fe/Ni metal-organic frameworks and their binder-free thin films for efficient oxygen evolution with low overpotential. *ACS Appl. Mater. Interfaces* **2016**, *8*, 16736–16743. [[CrossRef](#)]
13. Naguib, M.; Kurtoglu, M.; Presser, V.; Lu, J.; Niu, J.; Heon, M.; Hultman, L.; Gogotsi, Y.; Barsoum, M.W. Two-dimensional nanocrystals produced by exfoliation of Ti_3AlC_2 . *Adv. Mater.* **2011**, *23*, 4248–4253. [[CrossRef](#)] [[PubMed](#)]
14. Naguib, M.; Mochalin, V.N.; Barsoum, M.W.; Gogotsi, Y. 25th anniversary article: MXenes: A new family of two-dimensional materials. *Adv. Mater.* **2014**, *26*, 992–1005. [[CrossRef](#)]
15. Mashtalir, O.; Lukatskaya, M.R.; Zhao, M.Q.; Barsoum, M.W.; Gogotsi, Y. Amine-assisted delamination of Nb_2C MXene for li-ion energy storage devices. *Adv. Mater.* **2015**, *27*, 3501–3506. [[CrossRef](#)] [[PubMed](#)]
16. Xiong, D.; Li, X.; Bai, Z.; Lu, S. Recent advances in layered $\text{Ti}_3\text{C}_2\text{T}_x$ MXene for electrochemical energy storage. *Small* **2018**, *14*, 1703419. [[CrossRef](#)] [[PubMed](#)]

17. Ran, J.; Gao, G.; Li, F.T.; Ma, T.Y.; Du, A.; Qiao, S.Z. Ti₃C₂ MXene co-catalyst on metal sulfide photo-absorbers for enhanced visible-light photocatalytic hydrogen production. *Nat. Commun.* **2017**, *8*, 13907. [[CrossRef](#)]
18. Zhang, Q.; Teng, J.; Zou, G.; Peng, Q.; Du, Q.; Jiao, T.; Xiang, J. Efficient phosphate sequestration for water purification by unique sandwich-like MXene/magnetic iron oxide nanocomposites. *Nanoscale* **2016**, *8*, 7085–7093. [[CrossRef](#)]
19. Shahzad, F.; Alhabeib, M.; Hatter, C.B.; Anasori, B.; Hong, S.M.; Koo, C.M.; Gogotsi, Y. Electromagnetic interference shielding with 2D transition metal carbides (MXenes). *Science* **2016**, *353*, 1137–1140. [[CrossRef](#)]
20. Li, Z.; Zhuang, Z.; Lv, F.; Zhu, H.; Zhou, L.; Luo, M.; Zhu, J.; Lang, Z.; Feng, S.; Chen, W.; et al. The marriage of the FeN₄ moiety and MXene boosts oxygen reduction catalysis: Fe 3d electron delocalization matters. *Adv. Mater.* **2018**, *30*, 1803220. [[CrossRef](#)]
21. Wen, Y.; Rufford, T.E.; Chen, X.; Li, N.; Lyu, M.; Dai, L.; Wang, L. Nitrogen-doped Ti₃C₂T_x MXene electrodes for high-performance supercapacitors. *Nano Energy* **2017**, *38*, 368–376. [[CrossRef](#)]
22. Ammar, M.; Jiang, S.; Ji, S. Heteropoly acid encapsulated into zeolite imidazolate framework (ZIF-67) cage as an efficient heterogeneous catalyst for Friedel-Crafts acylation. *J. Solid State Chem.* **2016**, *233*, 303–310. [[CrossRef](#)]
23. Yu, M.; Zhou, S.; Wang, Z.; Zhao, J.; Qiu, J. Boosting electrocatalytic oxygen evolution by synergistically coupling layered double hydroxide with MXene. *Nano Energy* **2018**, *44*, 181–190. [[CrossRef](#)]
24. Wang, C.; Zhu, X.D.; Mao, Y.C.; Wang, F.; Gao, X.T.; Qiu, S.Y.; Le, S.R.; Sun, K.N. MXene-supported Co₃O₄ quantum dots for superior lithium storage and oxygen evolution activities. *Chem. Commun.* **2019**, *55*, 1237–1240. [[CrossRef](#)]
25. Tang, Y.; Yang, C.; Yang, Y.; Yin, X.; Que, W.; Zhu, J. Three dimensional hierarchical network structure of S-NiFe₂O₄ modified few-layer titanium carbides (MXene) flakes on nickel foam as a high efficient electrocatalyst for oxygen evolution. *Electrochim. Acta* **2019**, *296*, 762–770. [[CrossRef](#)]
26. Abbott, D.; Lebedev, D.; Waltar, K.; Povia, M.; Nachtegaal, M.; Fabbri, E.; Coperet, C.; Schmidt, T. Iridium oxide for the oxygen evolution reaction: Correlation between particle size, morphology, and the surface hydroxo layer from Operando XAS. *Chem. Mater.* **2016**, *28*, 6591–6604. [[CrossRef](#)]
27. He, P.; Yu, X.Y.; Lou, X.W. Carbon-incorporated nickel-cobalt mixed metal phosphide nanoboxes with enhanced electrocatalytic activity for oxygen evolution. *Angew. Chem. Int. Ed.* **2017**, *56*, 3897–3900. [[CrossRef](#)]
28. Chauhan, M.; Reddy, K.P.; Gopinath, C.S.; Deka, S. Copper cobalt sulfide nanosheets realizing a promising electrocatalytic oxygen evolution reaction. *ACS Catal.* **2017**, *7*, 5871–5879. [[CrossRef](#)]
29. Wen, Y.; Rufford, T.E.; Hulicova-Jurcakova, D.; Wang, L. Nitrogen and phosphorous co-doped graphene monolith for supercapacitors. *ChemSusChem* **2016**, *9*, 513–520. [[CrossRef](#)]
30. Li, H.; Yang, J.; Gao, M.; Wang, J.; Sun, B. Washing rice before cooking has no large effect on the texture of cooked rice. *Food Chem.* **2019**, *271*, 388–392. [[CrossRef](#)]
31. Wen, Y.; Rufford, T.E.; Hulicova-Jurcakova, D.; Zhu, X.; Wang, L. Structure control of nitrogen-rich graphene nanosheets using hydrothermal treatment and formaldehyde polymerization for supercapacitors. *ACS Appl. Mater. Interfaces* **2016**, *8*, 18051–18059. [[CrossRef](#)] [[PubMed](#)]
32. Wen, Y.; Wang, B.; Huang, C.; Wang, L.; Hulicova-Jurcakova, D. Synthesis of phosphorus-doped graphene and its wide potential window in aqueous supercapacitors. *Chem. Eur. J.* **2015**, *21*, 80–85. [[CrossRef](#)]

